LASER ISOLATION OF A CO2 PRE-AMPLIFIER ON AN EUVL SOURCE

by

Mark Wiley

A Master's Report Submitted to the Faculty of the

COLLEGE OF OPTICAL SCIENCE

In Partial Fulfillment of the Requirements

For the Degree of

MASTER OF SCIENCE

In the Graduate College

THE UNIVERSITY OF ARIZONA

2015

STATEMENT BY AUTHOR

This thesis has been submitted in partial fulfillment of requirements for an advanced degree at the University of Arizona and is deposited in the University Library to be made available to borrowers under rules of the Library.

Brief quotations from this thesis are allowable without special permission, provided that an accurate acknowledgement of the source is made. Requests for permission for extended quotation from or reproduction of this manuscript in whole or in part may be granted by the head of the major department or the Dean of the Graduate College when in his or her judgment the proposed use of the material is in the interests of scholarship. In all other instances, however, permission must be obtained from the author.

SIGNED: Mark Wiley

APPROVAL BY THESIS DIRECTOR

This thesis has been approved on the date shown below:

Jim Schwiegerling
Professor of Optical Sciences

December 3rd, 2015
Date

TABLE OF CONTENTS

LIST OF FIGURES

LIST OF TABLES

1 INTRODUCTION

1.1 REVIEW OF LITHOGRAPHY AND EUV

1.1.1 MOORE'S LAW

In 1975, Gordon Moore forecasted that semiconductor complexity would double about every two years[1]. Doubling the complexity is essentially the same as doubling the processing power or storage capacity without increasing the size of the chip. Or, keeping the same processing power or storage capacity, but reducing the size of the chip by half. This exponential growth over the past few decades has helped to enable the remarkable growth in technology related to smart phones, tablets, laptops, data storage, and many other electronics devices.

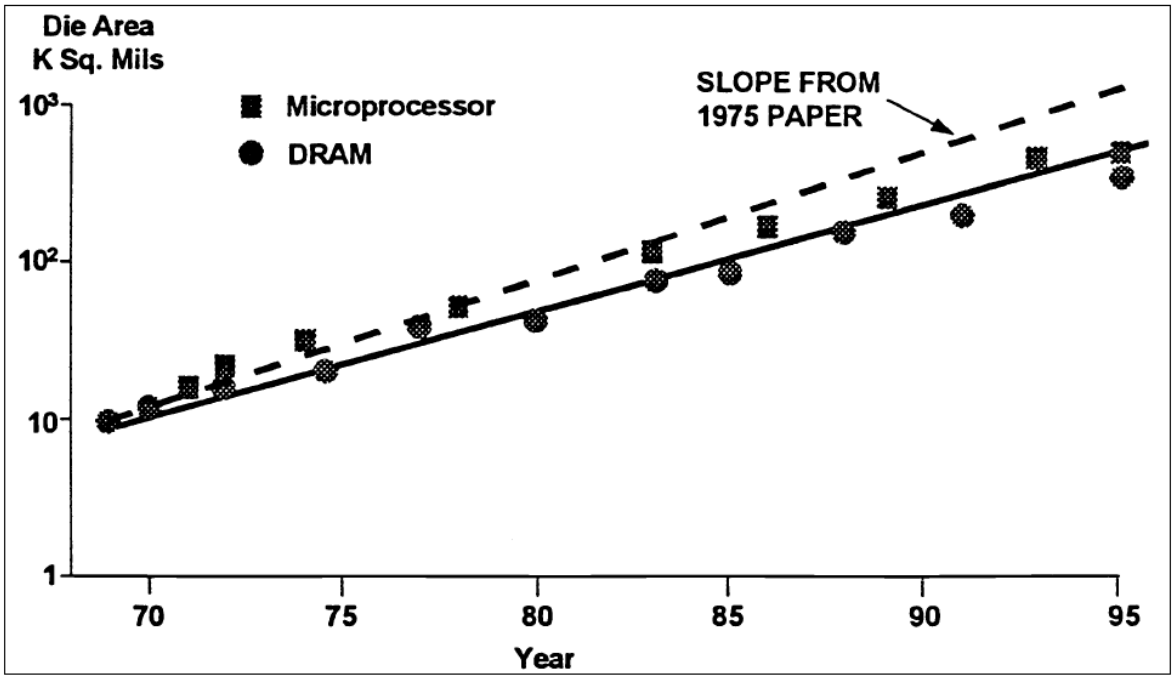

Figure 1.1 Moore's Projection From 1975 and 20 Years of Die Complexity Growth[1]

1.1.2 DUV LITHOGRAPHY

Photolithography is one of the technologies that have enabled Moore's Law to continue over the last several decades. Photolithography is a process in the manufacturing of integrated circuits, where light is used to transfer a pattern from a photomask onto a substrate/wafer. Ultra-Violet (UV) light is projected through a mask and then onto the photoresist on the substrate. The interaction of UV light with the photoresist etches the pattern of the mask into the substrate.

Lithography is widely used in the semiconductor industry because it is capable of creating very small structures (tens of nanometers) on silicon substrates which become small integrated circuits. The minimum feature size or Critical Dimension (CD) is limited by the wavelength of light, the Numerical Aperture (NA) of the projection optics, and the process constant (k_1) as shown in Equation (1)[2]. Shorter wavelength light is desirable, to allow for smaller feature sizes.

$$CD = k_1 \cdot \frac{\lambda}{NA} \tag{1}$$

In addition to CD, another important metric of a lithography system is the throughput. Throughput is typically expressed as Wafers per Hour (wph). Higher throughput leads to lower costs. Key limitations to throughput are the optical power of the source, and the sensitivity of the photoresist[3].

Argon fluoride (ArF) and krypton fluoride (KrF) Deep Ultraviolet (DUV) excimer lasers are the most common light sources currently used for photolithography in the semiconductor industry. ArF lasers operate at a wavelength of 193 nm, and KrF lasers operate at 248 nm. The short wavelength of the ArF, and the output power of up to 90 watts, allow for feature sizes smaller than 38 nm (using liquid immersion lithography) and throughput greater than 250 wph[4]. Cymer is the dominant supplier of excimer lasers for DUV lithography.

1.1.3 EXTENDING MOORE'S LAW WITH EUV

The International Technology Roadmap for Semiconductors (ITRS) predicts that Extreme Ultra-Violet Lithography (EUVL) is the technology that will likely take over from DUV lithography[5]. The use of a shorter wavelength for the lithography source is one way that Moore's Law can continue to be extended using photolithography. EUV has a wavelength of 13.5 nm. Because CD is proportional to the source wavelength, the 15x reduction in wavelength would significantly shrink the possible feature size. Chips made by EUVL could offer a 100-300% increase in storage capacity and processing power. This could enable smartphones to send and receive 4K video, and enable the storage of several terabytes of data on just one SD card[6].

However, EUVL has several technical challenges that must be overcome before it can become commercially viable. Every subsystem in the optical path must be re-engineered[3]. In addition to the new source to create the 13.5 nm light, new projection optics, reticles, and photoresists are needed. Because there are no suitable transmissive materials for EUV (including air) the

entire EUV optical path must change to ultra-high vacuum, and the illumination and projection optics and masks must all be reflective[7]. Mask infrastructure needs to be mature enough that a supply of defect free masks is available. Resists and post processing need to improve such that the chips meet performance targets[7]. Reflective projection optics with high NAs and acceptable optical loss are needed in the scanner. As shown in Figure 1.2, a huge industry-wide effort is ongoing to overcome these technical challenges and bring EUVL into High Volume Manufacturing (HVM).

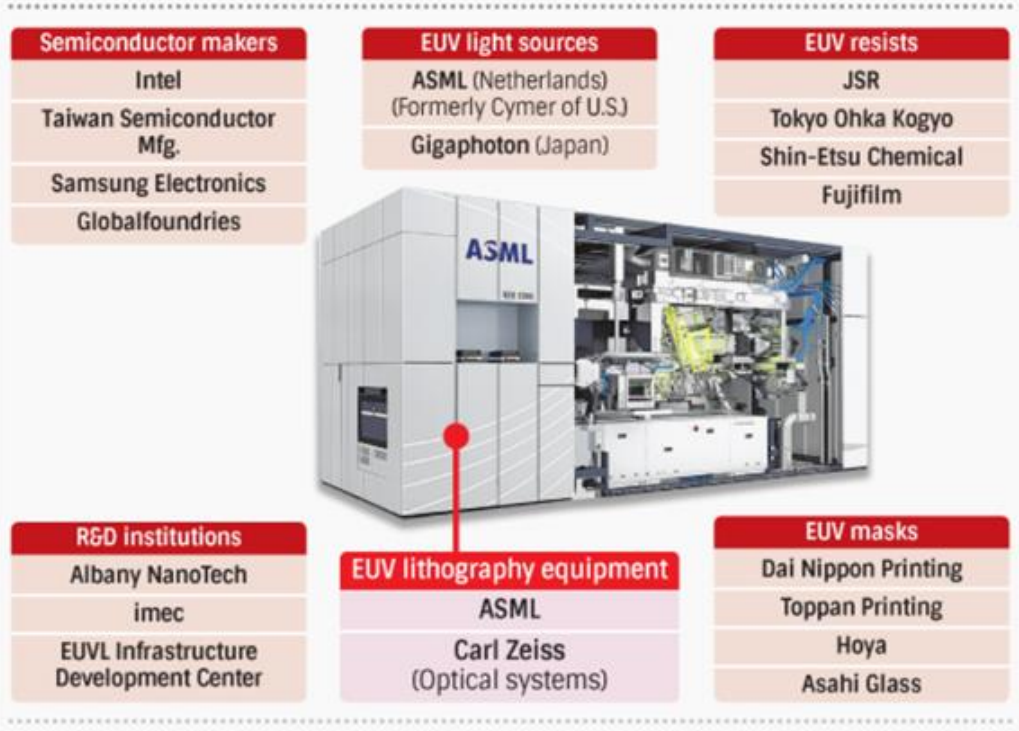

Figure 1.2 Companies Engaged in EUVL[6]

The EUV light source remains the most difficult challenge for EUVL[8]. A key challenge is achieving a high enough throughput to keep the costs reasonable. The transmission of light from the source to the wafer is very low since EUV mirrors have relatively low reflectivity.

Thin-film reflective coatings rely on refraction in each layer to ultimately increase the reflection of a bare substrate. When there are large differences in the refractive index of the alternating film layers, the reflectivity of the film stack is greater. Unfortunately for EUV wavelengths, most materials have refractive indices around $n \approx 1$.[9] With such small differences in refractive index between each layer, it is difficult to achieve very high reflection. Typically an EUV mirror is only about 60-70% reflective, as seen in Figure 1.3.

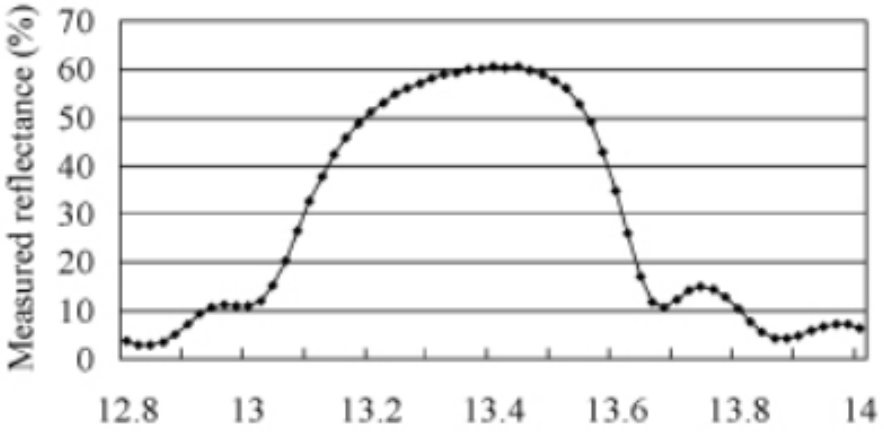

Figure 1.3 Typical EUV Mirror Reflectivity[9]

As shown in Figure 1.4 and Figure 1.5, a typical design of the EUV illumination and projection optics includes about 11 EUV mirrors. Since EUV mirrors have about 30% loss at each reflection, the transmission of light from the source to the wafer is only about 0.3%[10].

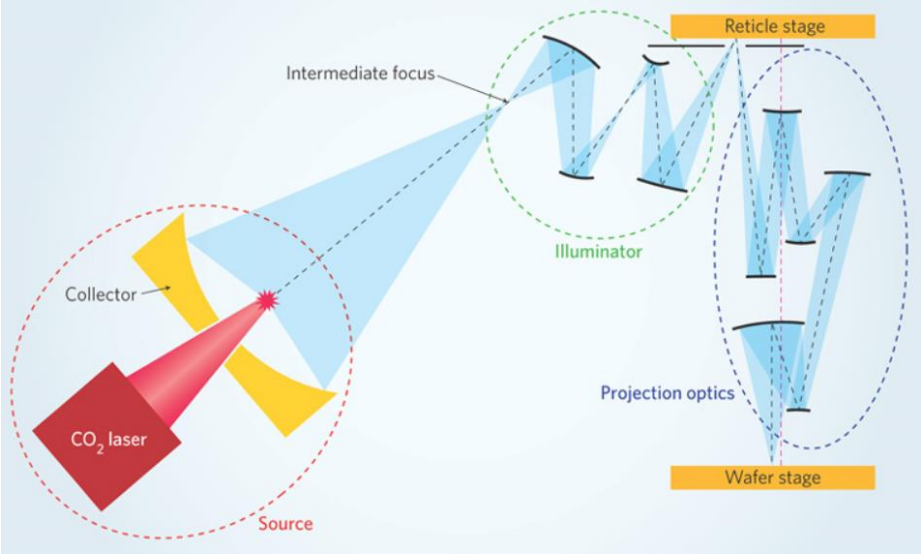

Figure 1.4 Example EUV Optical Path[11]

To achieve the throughput needed for HVM, 185 W of source power is needed[10]. High source power, along with mature source technology that provides for high reliability and uptime, are needed for EUVL to succeed. High source power will allow for throughput high enough to keep costs low. High reliability will enable the chip makers to consistently achieve the required throughput.

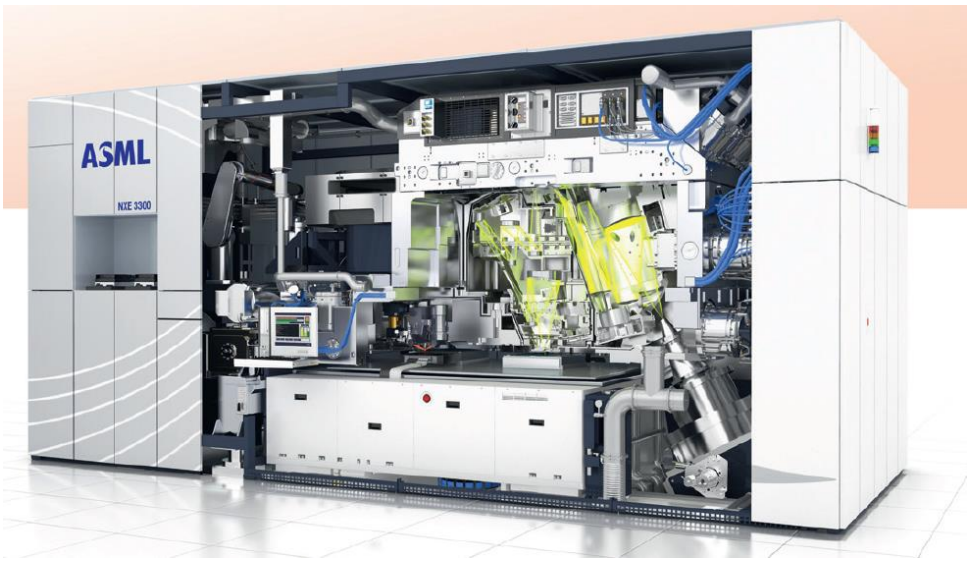

Figure 1.5 ASML NXE 3300 EUV Lithography Tool

1.2 OVERVIEW OF THE CYMER EUVL SOURCE

Cymer is the dominant supplier of EUV light sources. The Cymer EUV source uses the Laser Produced Plasma (LPP) method to generate the 13.5 nm radiation. LPP is the preferable method over Discharge Produced Plasma (DPP) for several reasons, including power scalability and smaller etendue[12].

Figure 1.6 shows the layout of the Cymer EUV source. The source consists of a high-power CO2 drive laser, a Beam Transport System (BTS), and a vacuum vessel where Sn droplets are supplied to the focus of the CO2 laser to generate EUV light. The drive laser is located in the sub-fab of the customer's facility, and the BTS is used to steer the high-power CO2 beam into the vacuum vessel which is located inside the ASML scanner[2]. Current generation Cymer sources use a pre-pulse technique, in which each Sn droplet is expanded with a pre-pulse just before being hit by the main pulse. The expansion of the droplet increases the efficiency at which the EUV is generated (conversion efficiency)[2, 13, 14]. The maximum predicted conversion efficiency is up to 6% [8].

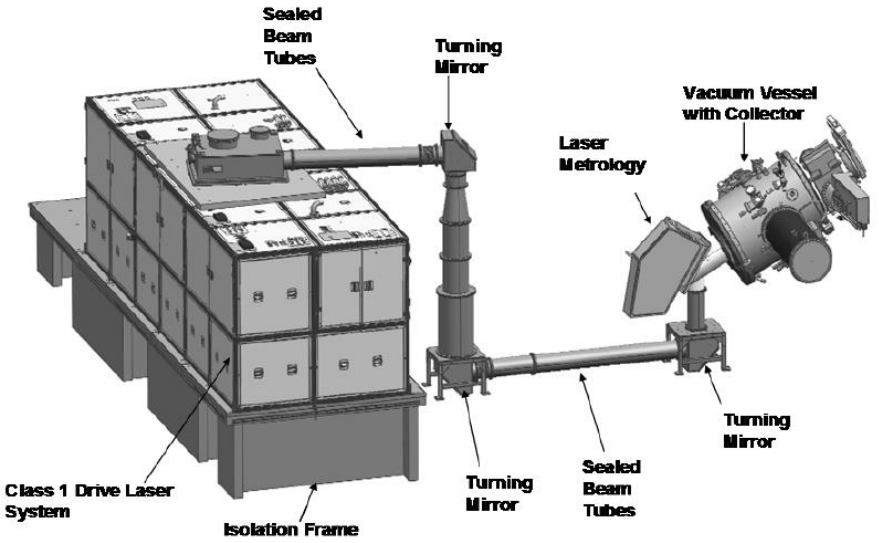

Figure 1: Scale Drawing of Laser Produced Plasma Source.

Figure 1.6 Scale Drawing of Laser Produced Plasma EUVL Source[13]

The drive laser consists of a Master Oscillator and Power Amplifier (MOPA) with a pre-pulse as shown in Figure 1.7. The CO2 (10.6 μm) beam originates from seed lasers in Master Oscillator (MO). The beam passes through a CO2 pre-amplifier before exiting the MO, and then enters the Power Amplifier (PA) chain. The PAs provide the majority of the amplification needed to reach sufficient power levels for EUV generation. The amplified beam is expanded as it enters the BTS to reduce the energy density on the steering mirrors[13] and then steered by the BTS from the exit of the PAs to the vacuum vessel. It is then focused at the first foci of an ellipsoidal collector mirror, to a waist diameter of about 100 μm[10]. A Sn droplet generator creates small (~30 μm) liquid Sn droplets at the same repetition rate as the pulsed laser. The droplets are first expanded by the laser pre-pulse, and then irradiated by the laser main pulse at the focal point of the laser. The laser pulses and the droplets are actively steered to maximize EUV generation[2].

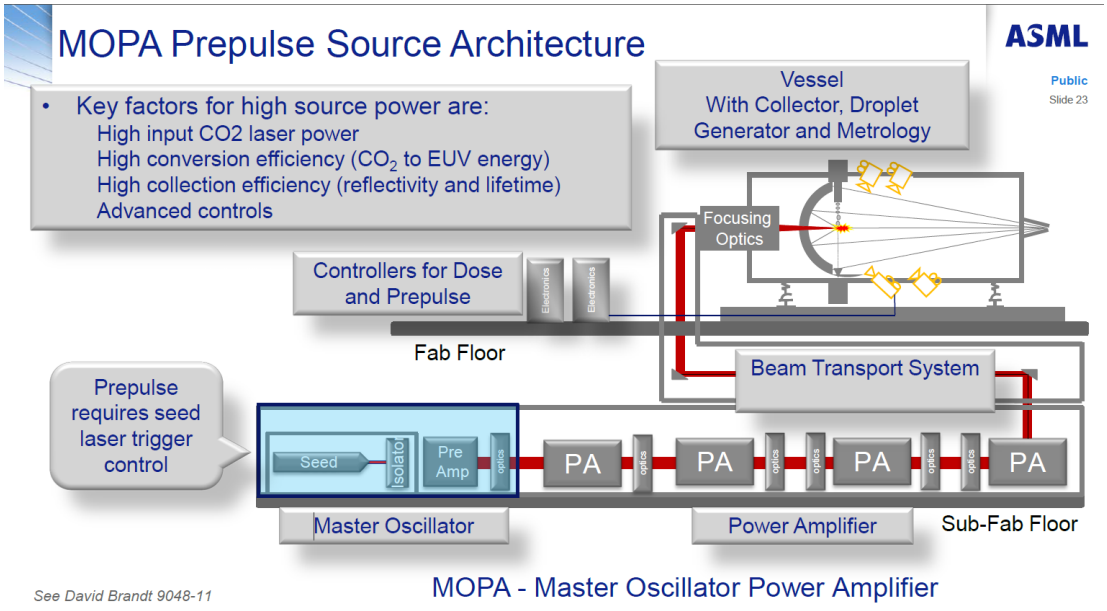

Figure 1.7 MOPA + Pre-pulse Architecture[15]

The high-power CO2 pulses (on the order of 1010 W/cm2) focused on the Sn droplets, create highly ionized plasmas that isotropically radiate EUV photons. The photons are collected by the ellipsoidal collector mirror and then focused to the Intermediate Focus (IF) where they are relayed to the projection optics in the scanner[10, 13]. The conversion efficiency (CE) of creating EUV using a CO2 beam is a critical factor in how much EUV power is achieved. With a CE of about 3%, more than 35 kW of CO2 power is needed to produce 185 W of EUV[13].

1.3 THE NEED FOR LASER ISOLATION

The pre-amplifier on the Cymer source is a high gain CO2 amplifier that is seeded from pulsed lasers. Self-lasing occurs when a laser cavity is formed when spontaneous emission is reflected from glint sources near the entrance and exit of the pre-amplifier. Additionally, reverse-propagating pulses originating further up the amplification chain can reenter the pre-amplifier causing parasitic lasing. Both self-lasing, and parasitic lasing, can lead to gain stripping of forward power, fluctuations of emitted power, or even laser damage of the cavity optics or surrounding optics.

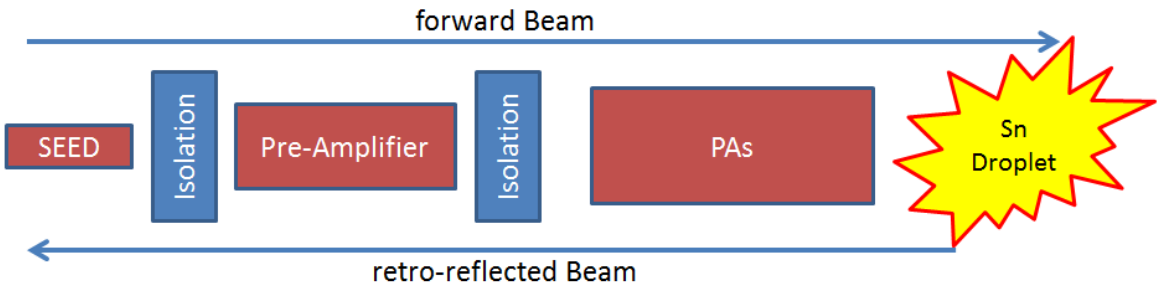

Figure 1.8 Simplified Optical Layout of the Amplification Chain on an LPP Source

Self lasing occurs when the optical gain of the cavity exceeds the sum of all the losses experienced in one round trip through the cavity[16]. To prevent self-lasing, an isolator is needed inside this cavity to reduce the energy in the glint reflections. Since the percent-reflection from glint sources is typically quite small, the isolator only needs to further reduce the reflected energy by about 10x.

When the forward-going pulse exits the pre-amplifier, it is further amplified by the PAs and eventually reaches the Sn droplet and creates EUV. Some CO2 energy is reflected from the

Sn droplet and then reenters the amplification chain headed in the reverse direction. An additional isolation scheme between the pre-amplifier and the PAs is intended to prevent the reverse pulse from reentering the pre-amplifier, but there is a small amount of energy that leaks through the isolator and reenters the pre-amplifier where it is again amplified. When this pulse exits the pre-amplifier in the reverse direction, small amounts of energy will be reflected from glint sources and will then travel again in the forward direction towards the input of the pre-amplifier. The isolator on the input side of the pre-amplifier is needed to prevent these pulses from reentering the amplification chain where they would cause gain stripping and eventually interfere with plasma creation at the Sn droplets. Because the pulse exiting the pre-amplifier in the reverse direction has much greater energy than the initial seed pulse, very high extinction is needed from the isolation scheme on the input side of the pre-amplifier. A target specification is that the energy in the glint reflection at the input of the pre-amplifier must be 100x less than the original seed pulse.

2 FIRST-ORDER DESIGN OF A LASER ISOLATOR

2.1 PRINCIPALS OF A QUARTER-WAVE ISOLATOR

A quarter-wave isolation scheme uses polarization components to pass the beam traveling in one direction but reject the reflected beam travelling in the opposite direction. Figure 2.1 shows a schematic of the isolation scheme at the entrance and exit of the pre-amplifier.

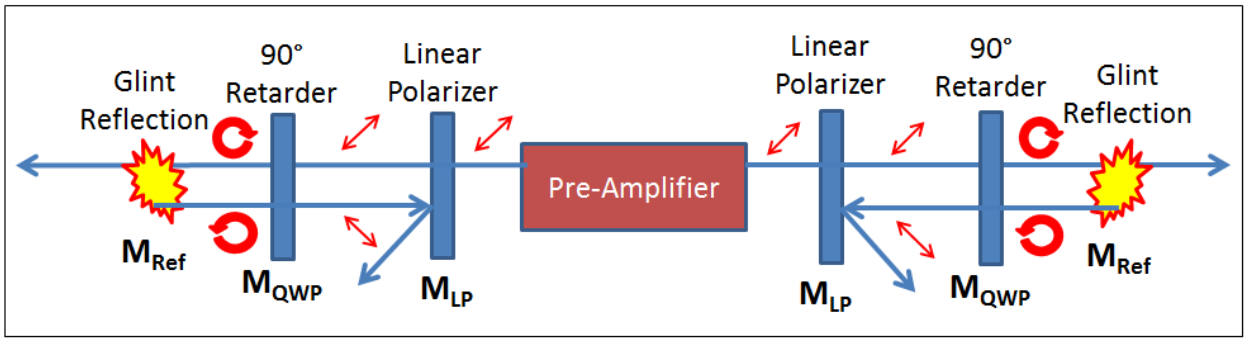

Figure 2.1 Optical Isolation of an LPP Pre-Amplifier

A linearly polarized beam travels through the pre-amplifier and then passes through a linear polarizer. The beam then encounters a 90° phase shift at the quarter-wave retarder, converting it into circular polarization. A reflection off a glint source or optical surface causes a handedness change. When the beam again encounters the 90° phase shift from the retarder, it returns to linear polarization but now in the orthogonal polarization state to the beam that exited the pre-amplifier. The linear polarizer now rejects the reflected beam, preventing it from reentering the pre-amplifier. Since there are both forward and reverse

propagating beams on the Cymer LPP source, the isolator scheme is used on each side of the pre-amplifier.

2.2 FIRST-ORDER ISOLATOR THORETICAL ANALYSIS

An optical isolator, consisting of a quarter-wave retarder and a linear polarizer, can be mathematically modeled using Mueller calculus. The polarization state of the input beam is represented by a Stokes vector, and the effects of each of the polarization components are represented by Mueller matrices. The Stokes vector of a beam at the output of a polarization element is calculated by the Mueller matrix of the element times the input Stokes vector, shown in Equation (2). The output Stokes vector represents the polarization state and relative intensity of the beam after passing through the polarization component.

$$S' = \begin{bmatrix} s_o{}' \\ s_1{}' \\ s_2{}' \\ s_3{}' \end{bmatrix} = MS = \begin{bmatrix} m_{00} & m_{01} & m_{02} & m_{03} \\ m_{10} & m_{11} & m_{12} & m_{13} \\ m_{20} & m_{21} & m_{22} & m_{23} \\ m_{30} & m_{31} & m_{32} & m_{33} \end{bmatrix} \begin{bmatrix} s_0 \\ s_1 \\ s_2 \\ s_3 \end{bmatrix} \quad (2)$$

For this analysis, the laser beam that exits the pre-amplifier and enters into the quarter-wave isolation components is considered the input beam. On the Cymer LPP source, this occurs in both the forward and reverse direction. The input Stokes vector is used to define the polarization state of this beam. Assuming a perfectly linearly polarized beam with its

polarization axis oriented at +45°, the Stokes vector for the input beam is represented by Equation (3).

$$S = \begin{bmatrix} s_0 \\ s_1 \\ s_2 \\ s_3 \end{bmatrix} = \begin{bmatrix} P_H + P_V \\ P_H - P_V \\ P_{45} - P_{135} \\ P_R - P_L \end{bmatrix} = \begin{bmatrix} 1 \\ 0 \\ 1 \\ 0 \end{bmatrix} \tag{3}$$

The Mueller matrix for an ideal polarizer, with its transmission axis at +45° is represented by Equation (4).

$$M_{LP+45} = \frac{1}{2}\begin{bmatrix} 1 & 0 & 1 & 0 \\ 0 & 0 & 0 & 0 \\ 1 & 0 & 1 & 0 \\ 0 & 0 & 0 & 0 \end{bmatrix} \tag{4}$$

The Mueller matrix for an ideal quarter-wave retarder oriented with its fast axis vertical is represented by Equation (5).

$$M_{QWP(v)} = \begin{bmatrix} 1 & 0 & 0 & 0 \\ 0 & 1 & 0 & 0 \\ 0 & 0 & 0 & -1 \\ 0 & 0 & 1 & 0 \end{bmatrix} \tag{5}$$

The Mueller matrix for a reflection is shown in Equation (6). This matrix changes the coordinate system of the reflected beam, and scales the intensity by the reflection coefficient (R). Since the beam in the quarter-wave isolator reflects off the glint source and then passes again through the retarder and linear polarizer, the coordinate systems for each component would need to be adjusted after the reflection from the glint source. For simplification, the

coordinate system changes can be ignored, and the glint source can be represented by the reflection coefficient alone as shown in Equation (7). This conveniently allows the same Mueller matrices for the retarder and linear polarizer to be used for the forward beam and reflected beam.

$$M_{Ref} = R\begin{bmatrix}1 & 0 & 0 & 0\\ 0 & 1 & 0 & 0\\ 0 & 0 & -1 & 0\\ 0 & 0 & 0 & -1\end{bmatrix} \tag{6}$$

$$M_{Ref} = R\begin{bmatrix}1 & 0 & 0 & 0\\ 0 & 1 & 0 & 0\\ 0 & 0 & -1 & 0\\ 0 & 0 & 0 & -1\end{bmatrix} \rightarrow R\begin{bmatrix}1 & 0 & 0 & 0\\ 0 & 1 & 0 & 0\\ 0 & 0 & 1 & 0\\ 0 & 0 & 0 & 1\end{bmatrix} = R \tag{7}$$

Additionally, since the net effect of passing through the quarter-wave retarder twice is the same as passing through a half-wave retarder once, the calculation can further be simplified by replacing the two Mueller matrices for the quarter-wave retarder with a single Mueller matrix for a half-wave retarder. The Mueller matrix for a half-wave retarder oriented with its fast axis vertical is shown in Equation (9).

$$M_{HWP(v)} = \begin{bmatrix}1 & 0 & 0 & 0\\ 0 & 1 & 0 & 0\\ 0 & 0 & -1 & 0\\ 0 & 0 & 0 & -1\end{bmatrix} \tag{8}$$

The leakage ($S_{Isolator}$) of a quarter-wave laser isolator represented mathematically using Mueller calculus (ignoring coordinate system changes on reflection) is shown in Equation (9).

It is the right-to-left product of the input stokes vector and each of the polarization components, scaled by the reflection coefficient of the glint source.

$$S_{Isolator} = (M_{LP+45} \cdot (R \cdot (M_{HWP(v)} \cdot (M_{LP+45} \cdot S)))) \quad (9)$$

The leakage % represents how much of the power that exits the pre-amplifier would reflect off a glint source and reenter the pre-amplifier going the opposite direction. Equation (10) shows that the % leakage is zero for the case of an ideal isolator, regardless of the value of R. The ideal isolation system provides full isolation of reflections from reentering the pre-amplifier.

$$S_{Isolator} = \frac{R}{4}\begin{bmatrix}1 & 0 & 1 & 0\\ 0 & 0 & 0 & 0\\ 1 & 0 & 1 & 0\\ 0 & 0 & 0 & 0\end{bmatrix} \cdot \left(\begin{bmatrix}1 & 0 & 0 & 0\\ 0 & 1 & 0 & 0\\ 0 & 0 & -1 & 0\\ 0 & 0 & 0 & -1\end{bmatrix} \cdot \left(\begin{bmatrix}1 & 0 & 1 & 0\\ 0 & 0 & 0 & 0\\ 1 & 0 & 1 & 0\\ 0 & 0 & 0 & 0\end{bmatrix} \cdot \begin{bmatrix}1\\ 0\\ 1\\ 0\end{bmatrix}\right)\right) = 0 \quad (10)$$

3 DESIGN OF THE LINEAR POLARIZER

3.1 TFP COATING DESIGN CONSIDERATIONS

A typical linear polarizer used in high-power laser systems is the Brewster plate Thin-Film Polarizer (Brewster TFP). Brewster TFPs take advantage of the difference in reflectance for S and P waves at oblique incidence. Materials for the thin-film layers are chosen to achieve very high reflectance of S polarization and very high transmittance of P polarization.[17] The Brewster angle is defined by Equation (11); for ZnSe (n=2.408) in air, the Brewster angle is 67.4°.

$$\theta_B = \tan^{-1}\left(\frac{n_2}{n_1}\right) \tag{11}$$

Brewster TFPs are characterized by performance parameters including transmittance of P polarization (Tp), the polarization ratio (Tp/Ts), %-absorption, and the Laser Induced Damage Threshold (LIDT). Several design choices influence these performance metrics, including coating materials, thicknesses, the number of coating layers, the deposition process, and the laser wavelength and pulse length.[18]

A common Brewster TFP coating consists of a multi-layer stack of alternating high and low index materials of quarter-wave optical thickness as shown in Equation (12).[19] This type of coating stack typically has overlapping regions of high reflectance of S polarization and high

transmittance of P polarization. The spectral width of the overlapping region depends on the refractive indices of the two coating materials. Typically the P polarization zone is spectrally lower than the S polarization zone. By tilting the plate at Brewster's angle, the transmission of P polarization is enhanced.[20]

$$Air\ |(HL)^N H|\ Substrate \tag{12}$$

For a single-wavelength TFP, Equation (13) can be used to estimate the number of coating layers needed to provide a desired polarization ratio P = (T_p/T_s). [21] Using ZnSe (n_H = 2.4028) and BaF2 (n_L = 1.3927), a desired polarization ratio of 100:1 at λ = 10.6 μm, and oriented at Brewster's angle (θ = 67.4°), the approximate number of coating layers is N = 9.

$$N = .05\left(\frac{n_H \cdot n_L}{n_H - n_L} \cdot \frac{\ln(2P)}{\sin\theta}\right) \tag{13}$$

Figure 3.1 shows that the required number of layers increases as the requirement for polarization ratio increases. It is intuitive that adding more coating layers will improve the polarization performance of the design. However in high-power laser applications this may also increase the thermal lensing since absorption is typically higher in the materials in the coating layers than in the bulk material of the substrate.

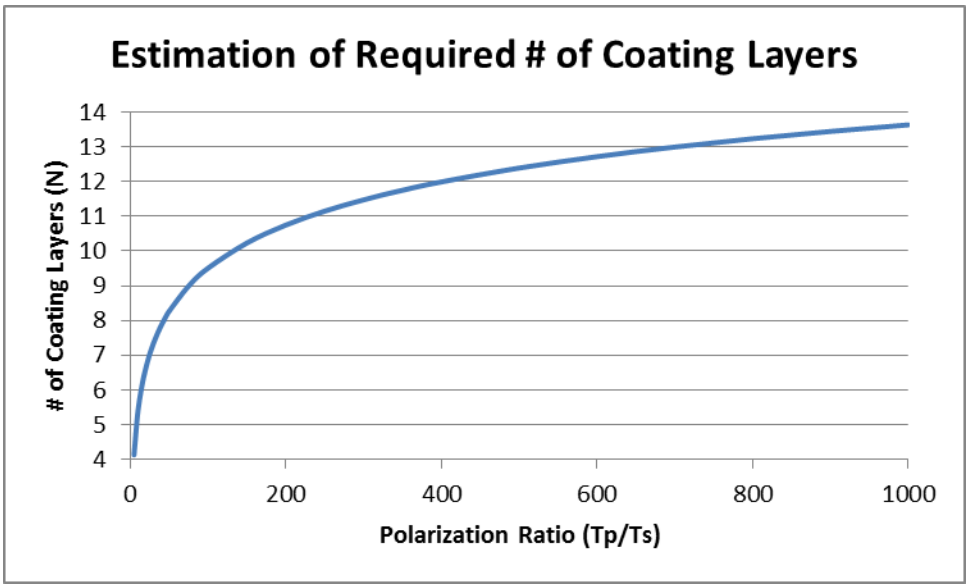

Figure 3.1 Estimated # of Coating Layers (N) For a Given Polarization Ratio

A tradeoff must be made to balance the polarization performance with the increased optical absorption resulting from added layers. Laser power absorbed in the coating heats the polarizer and leads to a thermal lensing effect on the transmitted laser beam. This can be particularly troublesome in Brewster TFPs since, due to the tilted plate, the thermal lensing effect will not be rotationally symmetric. The asymmetry can lead to astigmatism, which is difficult to compensate without the use of cylindrical optics.

Additionally, since the quarter-wave layers are fairly thick because of the long wavelength, the total physical thickness of the coating can be large. A very thick coating on one side of a plane-parallel plate adds stress to the optic that results in bending. Figure 3.2 shows an example of the bending of the TFP plate due to the stress from the TFP coating on one side of the optic.

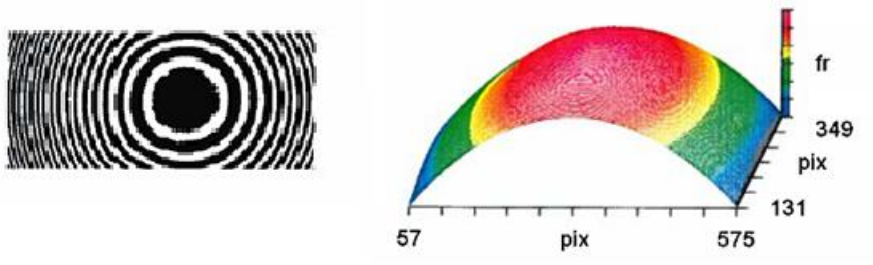

Figure 3.2 Lens Bending From Stress of TFP Coating

When used in transmission, the bending has only little impact. However if the TFP were to be used in reflection, the bending of the surface could have a significant focusing effect. In general, to reduce the absorbed power in the coating, and minimize surface bending, the minimum required coating layers should be used.

The Laser Induced Damage Threshold (LIDT) is an important metric of any coating used in a high-power laser system. The magnitude and profile of the electric field at each coating layer influences the damage morphology of that layer,[22] and can be examined to evaluate the overall LDIT capability of the design. High LDITs can be achieved by designing the coating to keep the peak electric field value low, and to locate the strongest electric field as far as possible from the incident medium (air). [18]

The general principle is to avoid peaks in the electric filed intensity at coating layer interfaces or within the high-index materials.[20] Since a Brewster TFP transmits nearly all of P polarization and reflects nearly all of S polarization, the electric field in the P polarization is typically of greater concern than that of the S polarization. Figure 3.3 shows an example of an electric field profile plot from Macleod Thin-Film design software for a TFP coating.

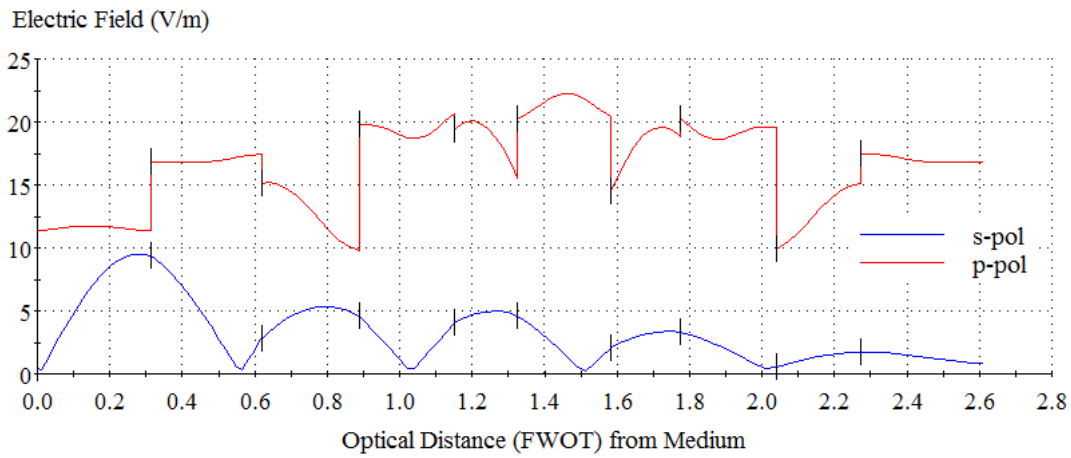

Figure 3.3 Example of a Polarization Dependent Standing-Wave Electric-Field Profile

If the electric field intensity peaks are located at interfaces or within the high-index material, the design can be improved by adding non-quarter-wave layers to the top of the coating stack. This can reduce the electric field at the layer interfaces and in the high-index material, which increases the threshold at which laser damage occurs.[22] To further increase the threshold for laser damage, materials with low absorption are chosen and the deposition process is performed with a focus on avoiding defects or contamination.[20]

3.2 EXAMPLE BREWSTER TFP COATING DESIGN FOR HIGH-POWER CO2 LASER WAVELENGTHS

In this section an example design of a thin-film TFP coating is presented. The design is based on typical materials used for CO2 laser applications, and multi-layer coating designs presented in referenced literature. This is not intended to be representative of any actual coatings used in the Cymer LPP source, although similarities could be present. The author does not have specific knowledge of the detailed coating design of any coatings used in the Cymer LPP Source.

Macleod thin-film design software was used to create a 10-layer alternating quarter-wave stack of ZnSe and BaF2 layers on a ZnSe substrate. The design of this coating is shown in Table 3.2. The optimization targets were high transmission of P-Polarization and high reflection of S-Polarization, for $\lambda = 10.6\ \mu m$. The simplex optimization method was used to refine the layer thicknesses. The transmission of P polarization is 99.8% and the transmission of S polarization is 0.77 % which provides a ratio (Tp/Ts) of 130.

Incident Angle (deg):			67.4
Reference Wavelength (μm):			10.6
Layer	Material	Refractive Index	Thickness (FWOT)
Medium	Air	1	
1	ZnSe	2.4028	0.3132
2	BaF2	1.3927	0.3051
3	ZnSe	2.4028	0.2692
4	BaF2	1.3927	0.2630
5	ZnSe	2.4028	0.1754
6	BaF2	1.3927	0.2562
7	ZnSe	2.4028	0.1941
8	BaF2	1.3927	0.2646
9	ZnSe	2.4028	0.2330
10	BaF2	1.3927	0.3346
Substrate	ZnSe	2.4028	

Table 3.1 TFP Single Wavelength Design

The achieved polarization ratio is somewhat better than expected based on Equation (18), although this design fails to meet the dual-wavelength requirements of the main-pulse/pre-pulse LPP system. When the coating design is further optimized to balance performance between the Main-Pulse and Pre-Pulse (PP) wavelengths (λ = PP & 10.6 μm), the polarization ratio decreases to 120 for λ = PP, and 57 for λ = 10.60 μm. It is immediately clear that more layers are needed to achieve a dual-wavelength polarization ratio of 100. 6 additional layers are added and the design is again refined to balance the performance between the two wavelengths. For the 16 layer design, Tp/Ts = 590 and 2500, for λ = 10.6 μm and PP

respectively. The spectral performance of the 10 and 16 layer coatings are shown in Figure 3.4.

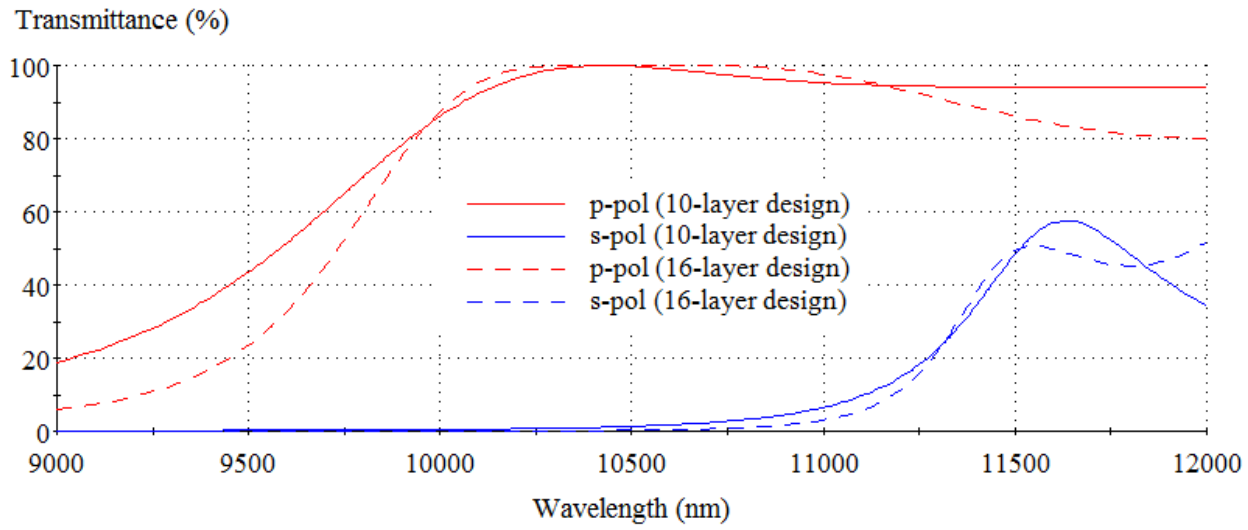

Figure 3.4 Spectral Performance of 10-Layer TFP Coating

For the sake of this example, a 14-layer coating shall be examined. 14 layers will achieve an acceptable dual-wavelength polarization ratio, without unnecessary layers that would increase the optical absorption. The detailed design of the 14-layer coating is shown in Table 3.2, and the transmittance spectrum is shown in Figure 3.5. At the PP wavelength, the transmission of P polarization is 99.57% and the transmission of S polarization is 0.12%, which gives a polarization ratio (Tp /Ts) of 830. At 10.6 μm, the transmission of P polarization is 99.77% and the transmission of S polarization is 0.491% which gives a polarization ratio of 200.

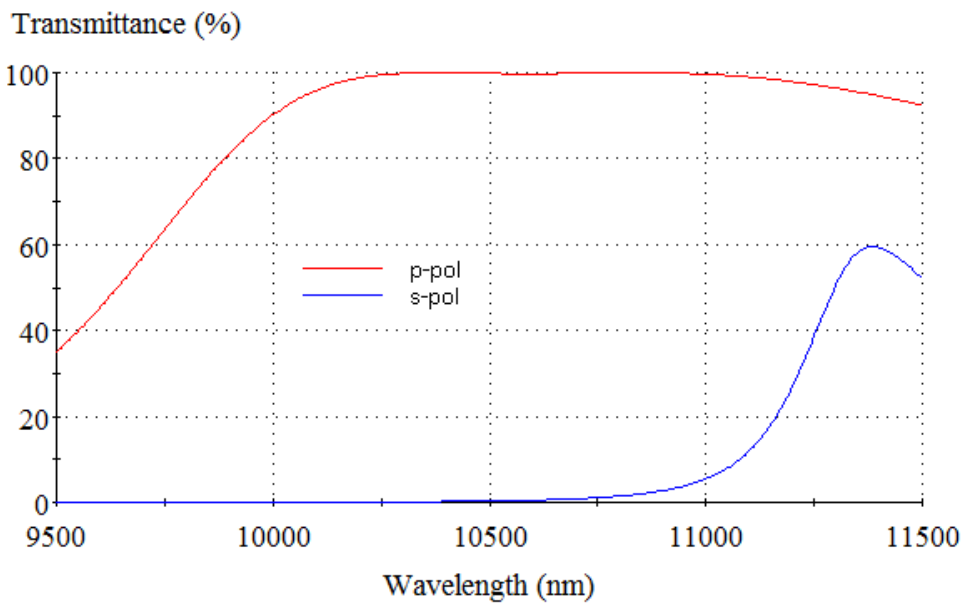

Figure 3.5 Spectral Performance of Refined 14-Layer TFP Design

Incident Angle (deg):			67.4
Reference Wavelength (μm):			10.6
Layer	Material	Refractive Index	Thickness (FWOT)
Medium	Air	1	
1	ZnSe	2.4028	0.3680
2	BaF2	1.3927	0.2788
3	ZnSe	2.4028	0.1770
4	BaF2	1.3927	0.2317
5	ZnSe	2.4028	0.1974
6	BaF2	1.3927	0.2637
7	ZnSe	2.4028	0.2350
8	BaF2	1.3927	0.2970
9	ZnSe	2.4028	0.2334
10	BaF2	1.3927	0.2716
11	ZnSe	2.4028	0.1884
12	BaF2	1.3927	0.2285
13	ZnSe	2.4028	0.1922
14	BaF2	1.3927	0.2682
Substrate	ZnSe	2.4028	

Table 3.2 Refined 14-Layer Dual Wavelength TFP Design

The theoretical polarization performance over a range of incident angles near Brewster's angle was calculated for each wavelength and plotted in Figure 3.6. It can be seen that the coating works well over a fairly wide range of angles near 67.4°.

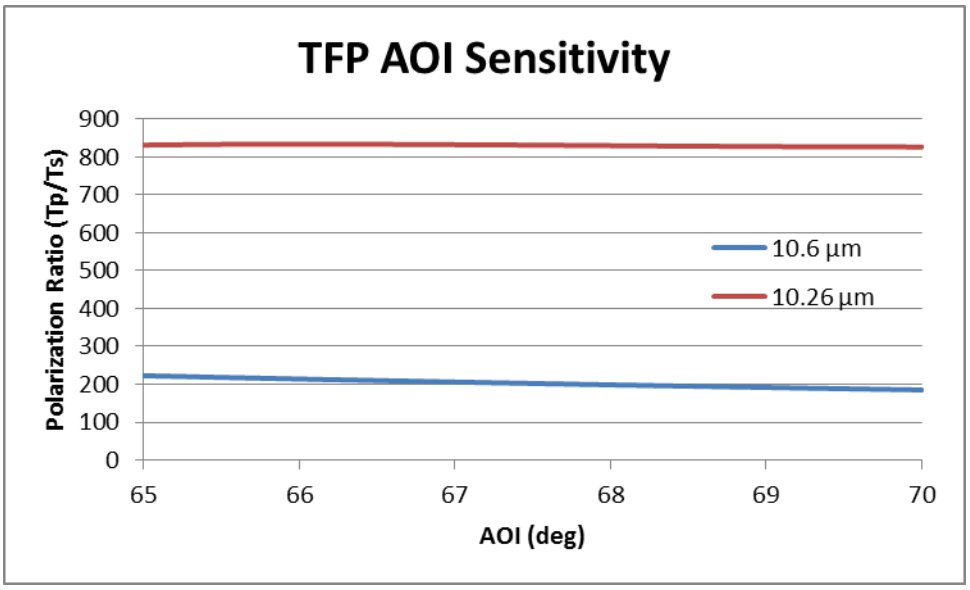

Figure 3.6 14-Layer TFP AOI Sensitivity

To evaluate the 14-layer design's sensitivity to LIDT, the electric field was plotted using Macleod software and is displayed in Figure 3.7. As expected, the electric field for S polarization decays quickly since most of S polarized light is reflected. Since the coating transmits almost all of P polarization, the average P polarized electric field remains high throughout the coating stack.

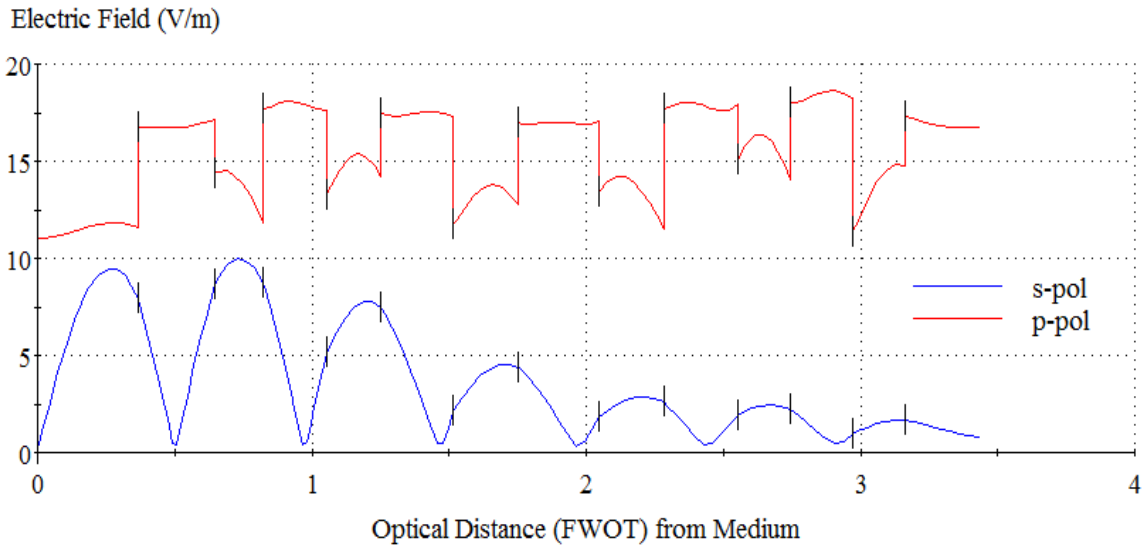

Figure 3.7 Electric-Field Profile of the 14-Layer TFP Design

Using the layer information in Table 3.2 as a reference, it can be seen that the highest intensity peaks in P polarization are located on the lower refractive index layers of BaF2. The opposite is true for S polarization; however the peak intensity of the electric field is smaller for S polarization than for P. As previously mentioned, an overcoat layer could be used to shift the intensity peaks if necessary, however that does not appear to be beneficial for this design.

The 14-layer design presented here is a good starting point for a Brewster TFP used in a high-power CO2 laser. A real design may be further optimized by changing the number of layers to match the specific requirements for polarization ratio and optical absorption. There are also other materials that may be chosen for the coating layers and substrate. The real design

must also include effects introduced by reflections off the back surface of the polarizer; this is discussed further in Section 4.1.1.

3.3 THERMAL CONSIDERATIONS IN THE TFP

When laser power is absorbed in the TFP coating as described in Section 3.1, a radial thermal gradient in the Brewster plate occurs. This gradient causes a variation in the refractive index of the substrate across the beam footprint, quantified by the change in refractive index with temperature (dn/dT)[23]. The refractive index gradient can be calculated from the temperature gradient, following Equation (14), where n' is the refractive index after temperature change, n is the refractive index before temperature change, ΔT is the temperature change, and dn/dT is the thermo-optic coefficient of the substrate. [24]

$$n' = n + \frac{dn}{dT}\Delta T \tag{14}$$

The variation in refractive index causes a lensing effect, which since the plate is tilted at Brewster's angle, introduces astigmatism in the laser beam. [25] The focal length of the thermal lens can be calculated using Equation (13), where κ is the thermal conductivity of the bulk material, A is the area of the beam profile, and P_{heat} is the optical power absorbed.

$$f^{-1} = \frac{dn/dT}{2\kappa A} P_{heat} \tag{15}$$

Accurate calculation of the optical power in the thermal lens depends on how well the value of the absorbed optical power is known. In the case of a high-power laser such as the Cymer LPP source, the laser power incident on the optic can vary with time and vary from system-to-system. In addition, it can be very difficult to quantify the sensitivity of the impact to system performance from the thermal lens. Because of these factors, it is difficult to assign a top-down specification. Instead, the design approach is to minimize thermal lensing by using rule-of-thumb design practices to remove the heat from the optic, and to minimize the absorbed power in the TFP coating by keeping the number of coating layers as small as required.

Power rejected by the TFP must be contained to a beam dump. It is convenient to attach the beam dump to the same mechanical mount as the TFP optic. However if there is insufficient thermal isolation between the beam dump and the optic, heat from the dump could transfer into the optic and cause a non-uniform temperature increase across the beam footprint. This added heat contributes further to the thermal lens.

To better understand the thermal gradients present, a Finite Element Analysis (FEA) of the Brewster TFP may be done.[23] An FEA provides information about peak temperatures, the temperature profile across the beam footprint, and the heat transfer between the beam dump and the optic. Figure 3.8 shows the FEA thermal profile of a TFP optic and an attached beam dump. There is heating both in the optic from absorption of the transmitted and reflected beam, and in the beam dump from the rejected S polarized beam.

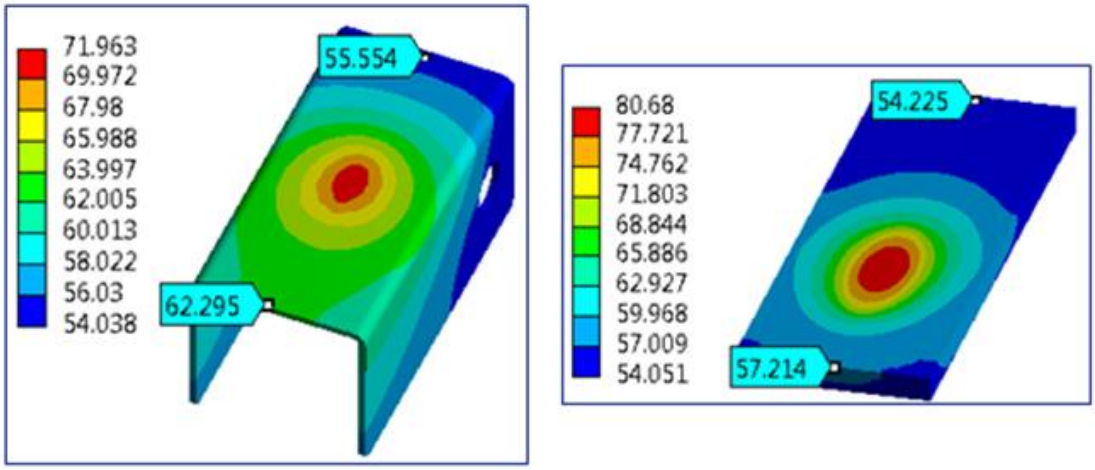

Figure 3.8 FEA Thermal Results for Initial TFP Concept

The accuracy of the FEA results depends heavily on the boundary conditions chosen in the model such as thermal conductivity at interfaces, input heat, and convection coefficients. Assumptions must be made for boundary conditions, and errors in the assumptions will certainly impact the accuracy of the results. In some cases experimental data may be used to calibrate certain boundary conditions in the FEA to increase the accuracy of the theoretical results.[23] However this does not solve the uncertainty due to power variations between different laser systems.

As a result of these uncertainties, it is difficult to have great confidence in the precision of the model. Using the model to predict temperature gradients, and then using those gradients to predict the focal length of the thermal lens, may not match very well to what is truly seen on a real system. The same can be true for calculations done using Equation (15).

However, the FEA can be very useful to make general design decisions based on relative differences between different concepts or designs. This is particularly helpful in the design of the TFP with an attached beam dump. It is intuitive to think that improving the thermal contact of the TFP to the mechanical mount will help remove the heat from the TFP. However, since the beam dump is also in contact with the mechanical mount, heat can actually transfer from the beam dump into the TFP. The solution in this case is to reduce the thermal contact between the dump and the mount; to reduce the amount of heat that transfers from the dump to the TFP.

Figure 3.9 shows the thermal profile of a modified design in which the peak temperatures of both the optic and the beam dump are reduced from what is shown in Figure 3.8. In the modified design, the coating has been redesigned with lower absorption, and the TFP optic has been thermally isolated from the heat in the beam dump. Additionally, the beam dump has been designed with better convection properties.

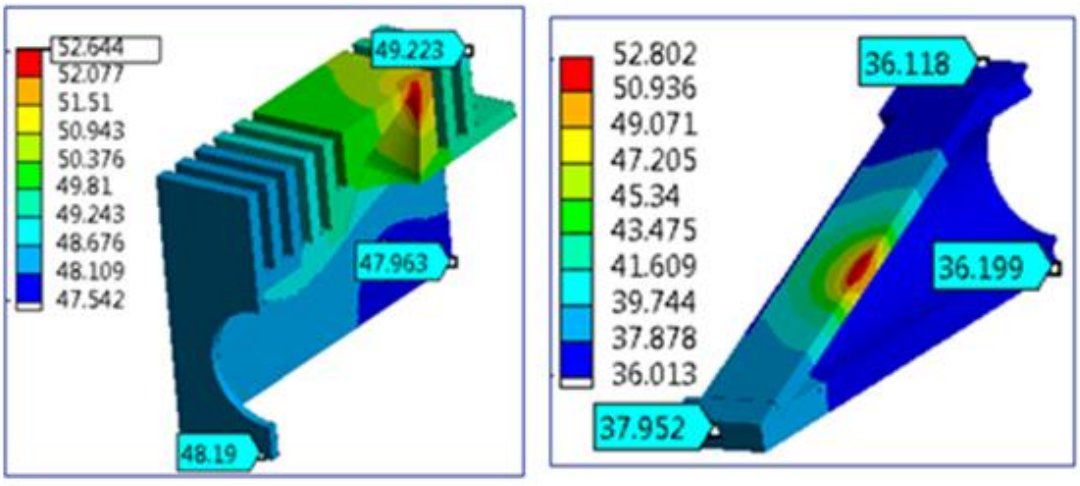

Figure 3.9 FEA Thermal Results for Improved TFP Concept

4 DESIGN AND TOLERANCING OF A REAL SYSTEM

4.1 ERRORS AND TOLERANCES

The first-order isolator calculations represent an ideal isolator, but of course there is no such ideal isolator. A real isolator will allow some of the glint energy to re-enter the pre-amplifier due to limitations or errors in the components or layout. Typical causes of non-ideal performance are phase error from the quarter-wave retarder, alignment errors, and coating limitations in the polarization components. When designing a real system, these errors must be understood and taken into account.

Alignment errors between the linear polarizer and the retarder reduce the isolation provided by the system. The orientation of the polarization axis of the polarizer must be 45° with respect to the fast-axis of the retarder. The polarization axis of the linear polarizer must also be aligned to match the input beam polarization state. However, errors with respect to the input polarization state will lead to loss of forward power, but not loss of isolation protection. Errors in the isolation scheme and loss of forward transmission are independent of each other; one cannot be used to compensate for the other.

4.1.1 ERRORS IN THE LINEAR POLARIZER

The general Mueller matrix for a linear polarizer is shown in Equation (16), where p_x and p_y are the orthogonal transmission coefficients. An ideal linear polarizer will reject all of one

polarization state (S-polarized) and pass all of the orthogonal state (P-polarized). For an ideal polarizer, $p_x = 0$ and $p_y = 1$ (or vice versa).

$$M_{POL}(p_x, p_y) = \frac{1}{2}\begin{bmatrix} {p_x}^2+{p_y}^2 & {p_x}^2-{p_y}^2 & 0 & 0 \\ {p_x}^2-{p_y}^2 & {p_x}^2+{p_y}^2 & 0 & 0 \\ 0 & 0 & 2p_xp_y & 0 \\ 0 & 0 & 0 & 2p_xp_y \end{bmatrix} \quad (16)$$

A real polarizer however will have a finite contrast ratio; a small amount of S-polarization is transmitted and a small amount of P-polarization is reflected. As shown in Section 3.2, design tradeoffs in the coating are made to balance between polarization performance and absorption, over the two wavelengths. Too much optical absorption can make the component prohibitive due to the effect of thermal lensing.

In addition to the non-ideal performance of the thin-film coating, errors can come from Fabry-Parot etalons. Etalons are caused by interference between the transmitted beam and the reflection from the back surface of the optic. In the case of a thin-film Brewster-plate polarizer used at CO2 laser wavelengths, the etalon effects can lead to unwanted transmission of the undesired polarization state. It is a small effect due to the large Angle of Incidence (AOI) and the small % reflection from the back surface, however it is significant due to the demanding isolation requirements. The analysis and design of the isolation system must include these effects in addition to the theoretical reflection and transmission coefficients for the thin-film coating itself.

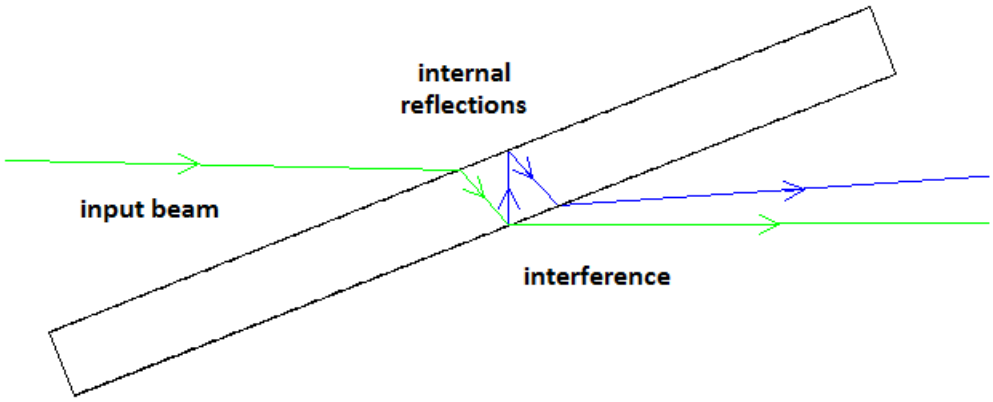

Figure 4.1 Etalon Effect in Thin-Film Polarizer

As shown in Figure 4.1, etalons occur from interference between the multiple reflections between the front and back surface of the polarizer. A coherent beam reflected from the back surface of the parallel plate interferes with the transmitted beam. The transmitted beam intensity is represented by Equation (17), where R_1 and R_2 are the reflection coefficients of each surface, and δ is the phase delay between the initial and the reflected beams.

$$I_T = I_0\left[1 - R_1 - R_2(1 - R_1)^2 - 2\sqrt{R_1 R_2}(1 - R_1) + 4\sqrt{R_1 R_2}(1 - R_1)\cos^2(\delta/2)\right] \quad (17)$$

$$\delta = \left(\frac{4\pi}{\lambda}\right) nt\cos\theta \quad (18)$$

Equation (18) shows that the phase delay (δ) is related to both the refractive index and the AOI. Because of this, the leakage through the polarizer will have both AOI and temperature sensitivity. Adding a slight wedge angle between the front and back surface of the plate can

nearly eliminate this sensitivity. Figure 4.2 shows the theoretical AOI sensitivity for a plate with no wedge compared to the same plate with a 4 arcminute wedge. It is clear that the sensitivity is eliminated, but that the average magnitude over the range of AOI is unchanged. In principle, if the AOI is well controlled on the system, the polarizer could be tilted to optimize rejection of the undesired polarization state. In practice though, it may be more desirable to eliminate the sensitivity.

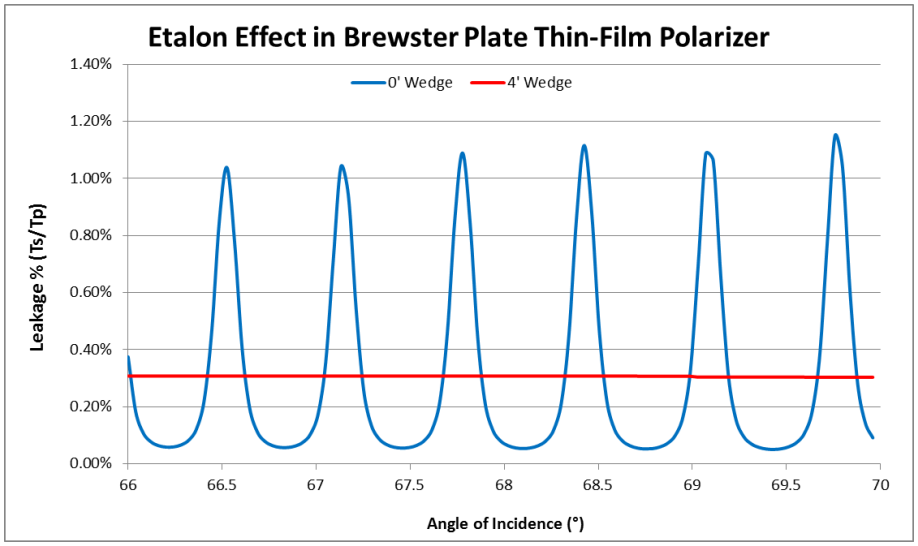

Figure 4.2 Etalon AOI Sensitivity Modeled in FRED

Figure 4.3 Shows the etalon sensitivity to temperature changes. Since the refractive index and the physical thickness of the optic both vary as a function of temperature, the leakage through the polarizer is temperature dependent. If the temperature of the optic could be well controlled, in principle the thickness could be chosen to minimize the leakage. However in the case of a high-power laser system, the preferred solution is to eliminate the sensitivity using a slight wedge.

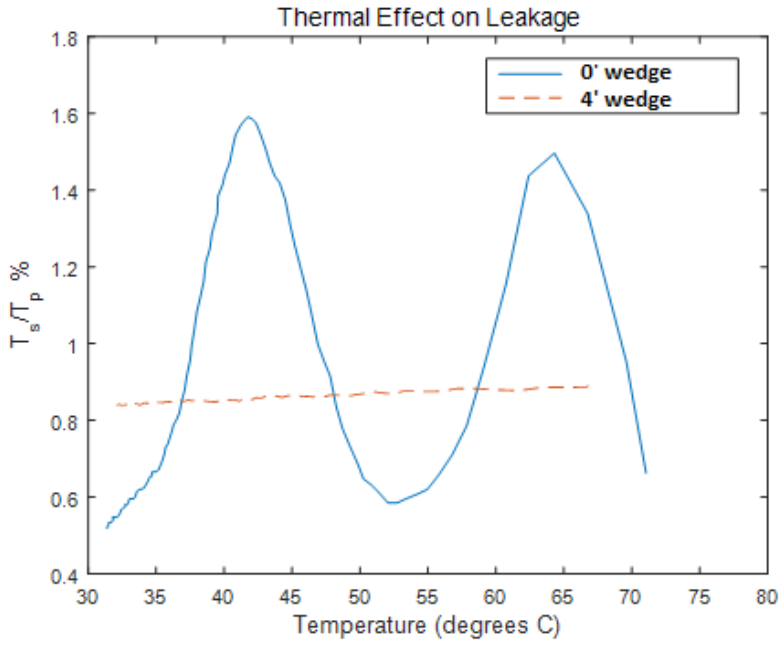

Figure 4.3 Etalon Thermal Sensitivity

Representing the non-ideal nature of a real thin-film coating and the leakage from etalons, the Mueller matrix for a thin-film Brewster plate polarizer with a contrast ratio of ~50:1 (p_x = 0.02 and p_y = 0.97) rotated at +45° is shown in Equation (19).

$$M_{TFP(+45)} = \frac{1}{2}\begin{bmatrix} {p_x}^2+{p_y}^2 & 0 & {p_y}^2-{p_x}^2 & 0 \\ 0 & 2p_xp_y & 0 & 0 \\ {p_y}^2-{p_x}^2 & 0 & {p_x}^2+{p_y}^2 & 0 \\ 0 & 0 & 0 & 2p_xp_y \end{bmatrix} = \frac{1}{2}\begin{bmatrix} 0.9413 & 0 & 0.9405 & 0 \\ 0 & 0.0388 & 0 & 0 \\ 0.9405 & 0 & 0.9413 & 0 \\ 0 & 0 & 0 & 0.0388 \end{bmatrix} \quad (19)$$

4.1.2 ERRORS IN THE QUARTER-WAVE RETARDER

In the case of a dual-wavelength Main-Pulse/Pre-Pulse setup (as in the Cymer system) phase error in the quarter-wave retarder can come from non-ideal coating performance (a dual-band phase retarding coating). The coating may be optimized for one wavelength, but have some error in the other wavelength or the error may be balanced between the two wavelengths. Phase error can also be caused by angle of incidence sensitivity/error. This is particularly true for thin-film based reflective phase retarders that are used in the Cymer system. There will be some deviation from a quarter-wave of retardance.

The Mueller matrix of a wave plate (fast axis θ, retardance δ) is shown in Equation (20) . In the ideal case ($\delta = 90°$, $\theta = 90°$), a quarter-wave plate oriented vertically can be represented simply by Equation (5). In practice though, quarter-wave plates have a certain amount of phase error, either from non-ideal coating performance, manufacturing tolerances, or AOI sensitivity.

$$M_{QWP} = \begin{bmatrix} 1 & 0 & 0 & 0 \\ 0 & \cos^2 2\theta + \sin^2 2\theta \cos\delta & \sin 2\theta \cos 2\theta\,(1-\cos\delta) & -\sin 2\theta \sin\delta \\ 0 & \sin 2\theta \cos 2\theta\,(1-\cos\delta) & \sin^2 2\theta + \cos^2 2\theta \cos\delta & \cos 2\theta \sin\delta \\ 0 & \sin 2\theta \sin\delta & -\cos 2\theta \sin\delta & \cos\delta \end{bmatrix} \quad (20)$$

It is assumed that the polarizer is rotated exactly at 45 degrees (the same orientation of the incoming beam polarization). In a real system there would be some orientation error. However, as discussed in Section 4.1, this error is unrelated to the extinction of the isolation

system. The alignment error of interest for this analysis is the rotational error between the quarter-wave retarder and the linear polarizer; this error is represented by θ in Equation (20).

4.2 TRUE PERFORMANCE OF A REAL SYSTEM

The first order design and analysis presented in Section 2.2 is a good start for designing an isolation scheme, and in some cases it may be sufficient to stop there. However in high-power laser systems with demanding requirements for laser isolation, a complete analysis of the true performance must be considered. This analysis must take into account the errors discussed in the previous sections including non-ideal coating performance, thermal issues, and alignment sensitivities. This analysis can be performed with modified Mueller matrices that include the actual polarization influences of each component.

Equation (9) is used again, however now using the Mueller matrices for real components, shown Equations (19) and (20). Results of this analysis can be used to evaluate system performance bottom-up to understand what level of isolation can be expected with existing components. It can also be used to create a top-down optical and mechanical tolerance budget to design a real system that achieves the desired level of isolation.

For an example, an isolation system has been modeled with a design target that glint reflections reentering the pre-amplifier must be 100x lower intensity than the original forward going pulses (as discussed in Section 1.3). This leads to an isolation requirement of $1.25 \times 10^{-}$

[5], based on typical power levels seen for forward and reverse beams on the Cymer source. Common anti-reflection coatings at CO2 wavelengths have reflections of around 0.2 % per surface. Other sources of glint may reflect much more, but for the purpose of this example the reflection coefficient (R) shall be 0.002.

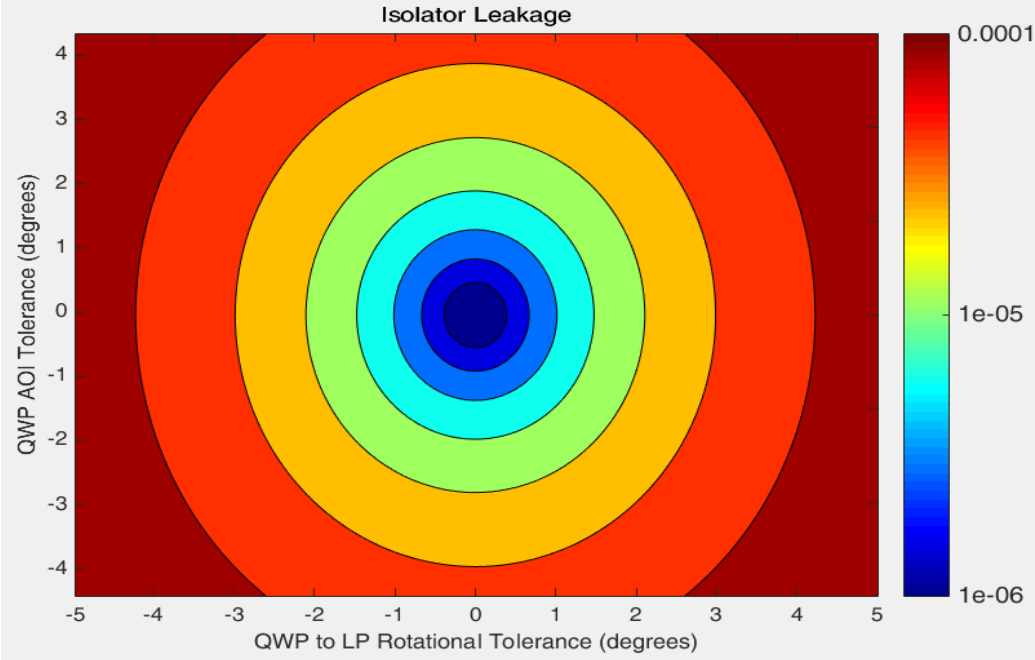

Figure 4.4 Isolator Leakage – Sensitivity to AOI and Rotation

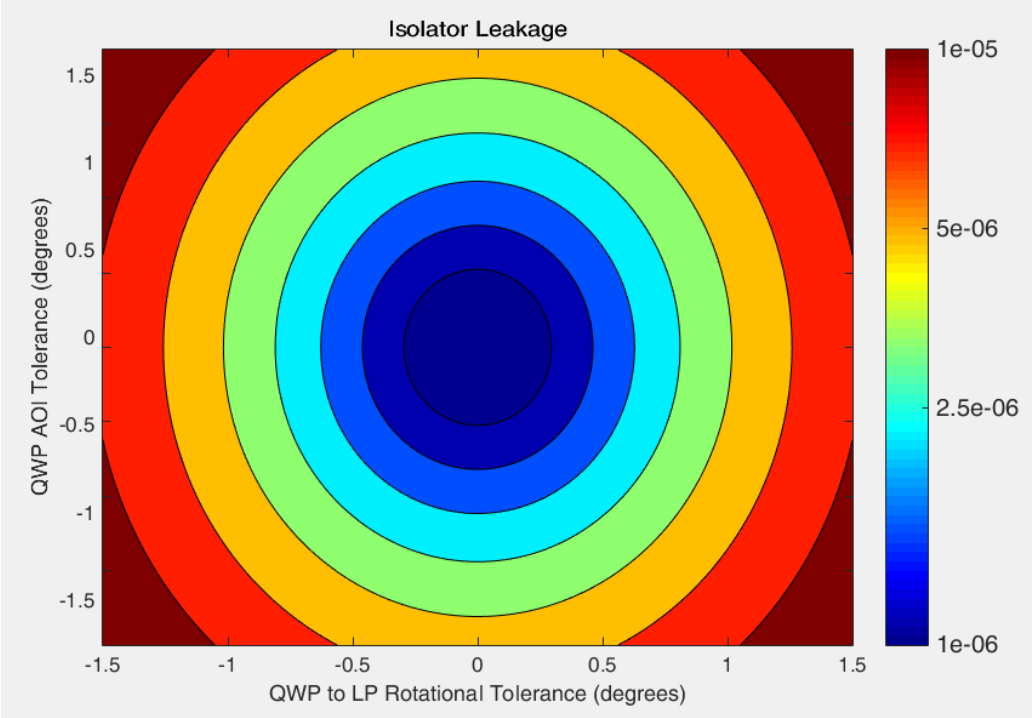

Figure 4.5 Isolator Leakage – Sensitivity to AOI and Rotation (zoomed-in)

Figure 4.4 shows the calculated leakage for a real system over a range of AOI and rotational errors. Conveniently, the sensitivities to AOI and rotational errors are similar enough that they can be plotted on the same scale. The results show that to keep leakage below the level of 1.25×10^{-5}, the AOI and rotational tolerances must be held to within about ± 1.5°. Since all of the optical error (coatings, polarization, phase errors) have already been accounted for in the analysis, the entire ± 1.5° can be budgeted for the mechanical mounts, and the beam alignment into the isolator. Also shown in Figure 4.4 is the same calculated data plotted on a smaller scale. It can be seen that if the mechanical and beam alignment tolerances could be held to within ± 0.5°, then leakage could be reduced to below 1×10^{-6}.

5 SUMMARY

Several technical challenges must be overcome before commercially viable EUVL power levels can be achieved. One aspect of scaling EUV power is to scale the power in the CO2 laser. The demand for higher CO2 laser power increases the need for laser isolation of the preamplifier from glint reflections and reverse-propagating laser pulses.

The methods described in this report can be used to design a quarter-wave optical isolation scheme suitable for the demanding requirements of the CO2 laser in an EUVL source. It has been shown that the design work involves balancing several parameters to achieve the desired isolation for each wavelength without introducing prohibitive levels of thermal lensing or requiring unachievable alignment or mechanical tolerances.

The Mueller calculus analysis shown is used to understand the combined impact of each of the design variables. The analysis can be used to understand the performance and sensitivities of an existing system, or to create a top-down tolerance budget for a new design based on a desired level of isolation.

6 REFERENCES

[1] Moore, G. E., [Lithography and the Future of Moores Law], 17 (1995).

[2] Brandt, D. C., Fomenkov, I. V., La Fontaine, B. M. and Lercel, M. J. , "Laser-Produced Plasma Light Sources for EUV Lithography," Solid State Technol. 55(5), 26-28 (2012).

[3] Sivakumar, S., [EUV Lithography: Prospects and Challenges], 402 (2011).

[4] http://www.asml.com , "TWINSCAN NXT:1970Ci," 2015(August, 21).

[5] Ronse, K., De Bisschop, P., Vandenberghe, G., Hendrickx, E., Gronheid, R., Pret, A. V., Mallik, A., Verkest, D. and Steegen, A. , "Opportunities and challenges in device scaling by the introduction of EUV lithography," 2012 Ieee International Electron Devices Meeting (Iedm) (2012).

[6] Hosokwaw, K. and Kimura, M. , "Breakthrough puts 10-nanometer chips within reach by 2017," (2015).

[7] http://www.itrs.net/ , "2013Litho_Summary.pdf," 2015(August 8).

[8] Wurm, S. , "EUV Lithography," Proceedings of Technical Program - 2014 International Symposium on Vlsi Technology, Systems and Application (Vlsi-Tsa) (2014).

[9] H. J. Levinson, [*Principles of Lithography, Second Edition*], SPIE PRESS, Bellingham, WA (2005).

[10] Fomenkov, I. V., La Fontaine, B., Brown, D., Ahmad, I., Baumgart, P., Boewering, N. R., Brandt, D. C., Bykanov, A. N., De Dea, S., Ershov, A. I., Farrar, N. R., Golich, D. J., Lercel, M. J., Myers, D. W., Rajyaguru, C., Srivastava, S. N., Tao, Y. and Vaschenko, G. O. , "Development of stable extreme-ultraviolet sources for use in lithography exposure systems," Journal of Micro-Nanolithography Mems and Moems 11(2), 021110 (2012).

[11] Christian Wagner & Noreen Harned , "EUV lithography: Lithography gets extreme," Nature Photonics 4, 24 (2010).

[12] www.cymer.com , "http://www.cymer.com/euv-lithography/why-lpp," 2015(September 9).

[13] Brandt, D. C., Fomenkov, I. V., Lercel, M. J., La Fontaine, B. M., Myers, D. W., Brown, D. J., Ershov, A. I., Sandstrom, R. L., Bykanov, A. N., Vaschenko, G. O., Boewering, N. R., Das, P., Fleurov, V. B., Zhang, K., Srivastava, S. N., Ahmad, I., Rajyaguru, C., De Dea, S., Dunstan, W. J., Baumgart, P., Ishihara, T., Simmons, R. D., Jacques, R. N., Bergstedt, R. A., Porshnev, P. I., Wittak, C. J., Woolston, M. R., Rafac, R. J., Grava, J., Schafgans, A. A. and Tao, Y. , "Laser Produced Plasma EUV Sources for Device Development and HVM," Extreme Ultraviolet (Euv) Lithography Iii 8322, 83221I (2012).

[14] Peeters, R., Lok, S., Mallman, J., van Noordenbrug, M., Harned, N., Kuerz, P., Lowisch, M., van Setten, E., Schiffelers, G., Pirati, A., Stoeldraijer, J., Brandt, D., Farrar, N., Fomenkov, I., Boom, H., Meiling, H. and Kool, R. , "EUV lithography: NXE platform performance overview," Extreme Ultraviolet (Euv) Lithography V 9048, 90481J (2014).

[15] www.asml.com , "http://www.asml.com/doclib/misc/asml_20140306_EUV_lithography_-_NXE_platform_performance_overview.pdf;" 2015(09/14).

[16] Wikipedia , "https://en.wikipedia.org/wiki/Lasing_threshold,".

[17] COJOCARU, E. , "Comparison of Theoretical Performances for Different Single-Wavelength Thin-Film Polarizers," Appl.Opt. 31(22), 4501-4504 (1992).

[18] Meiping Zhu, Kui Yi, Zhengxiu Fan and Jianda Shao , "Theoretical and experimental research on spectral performance and laser induced damage of Brewster's thin film polarizers," Appl.Surf.Sci. 257(15), 6884; 6884-6888; 6888 (2011).

[19] Cojocaru, E., Dragulinescu, D., Grigoriu, C. and Julea, T. , "Computer analysis of multilayer thin-film polarizers at 10.6 mum on ZnSe and KCl substrates at Brewster angle of incidence," Rev.Roum.Phys. 34(2), 211; 211-216; 216 (1989).

[20] Sahraee, M., Fallah, H. R., Moradi, B., Zabolian, H. and Mahmoodzade, M. H. , "Design and fabrication of thin-film polarizer at wavelength of 1540 nm and investigation of its laser-induced damage threshold," Eur.Phys.J.Plus 129(12), 1-6 (2014).

[21] BLANC, D., LISSBERGER, P. and ROY, A. , "Design, Preparation and Optical Measurement of Thin-Film Polarizers," Thin Solid Films 57(1), 191-198 (1979).

[22] Stolz, C. , "Brewster's angle thin film plate polarizer design study from an electric field perspective," Advances in Optical Interference Coatings 3738, 347-353 (1999).

[23] Paschotta, R. , "www.rp-photonics.com," 2015(11/20).

[24] Vukobratovich, D., [Introduction to Opto-Mechanical Design] (2008).

[25] SINCLAIR, D. , "Optical Loss and Thermal Distortion in Gas-Laser Brewster Windows," Appl.Opt. 9(4), 797-& (1970).

[26] II-VI Infrared , "http://www.iiviinfrared.com/CO2-Laser-Optics/thin-film-polarizers.html," 2015(10/01).